



LAWRENCE
LIVERMORE
NATIONAL
LABORATORY

Accessing Ultra-High Pressure, Quasi-Isentropic States of Matter

K. T. Lorenz, M. J. Edwards, S. G. Glendinning, D. D.
Ho, A. F. Jankowski, J. McNaney, S. M. Pollaine, B. A.
Remington

November 17, 2004

46th Annual Meeting of the Division of Plasma Physics
Savannah, GA, United States
November 15, 2004 through November 19, 2004

Disclaimer

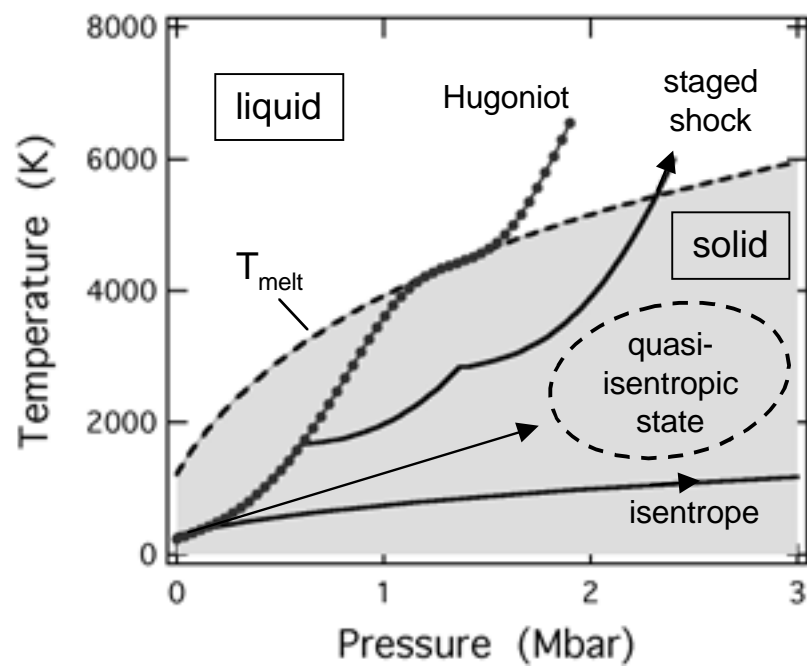
This document was prepared as an account of work sponsored by an agency of the United States Government. Neither the United States Government nor the University of California nor any of their employees, makes any warranty, express or implied, or assumes any legal liability or responsibility for the accuracy, completeness, or usefulness of any information, apparatus, product, or process disclosed, or represents that its use would not infringe privately owned rights. Reference herein to any specific commercial product, process, or service by trade name, trademark, manufacturer, or otherwise, does not necessarily constitute or imply its endorsement, recommendation, or favoring by the United States Government or the University of California. The views and opinions of authors expressed herein do not necessarily state or reflect those of the United States Government or the University of California, and shall not be used for advertising or product endorsement purposes.

Accessing Ultra-High Pressure, Quasi-Isentropic States of Matter

K. T. Lorenz, M. J. Edwards, S.G. Glendinning, A. F. Jankowski,
J. McNaney, S. M. Pollaine, B. A. Remington

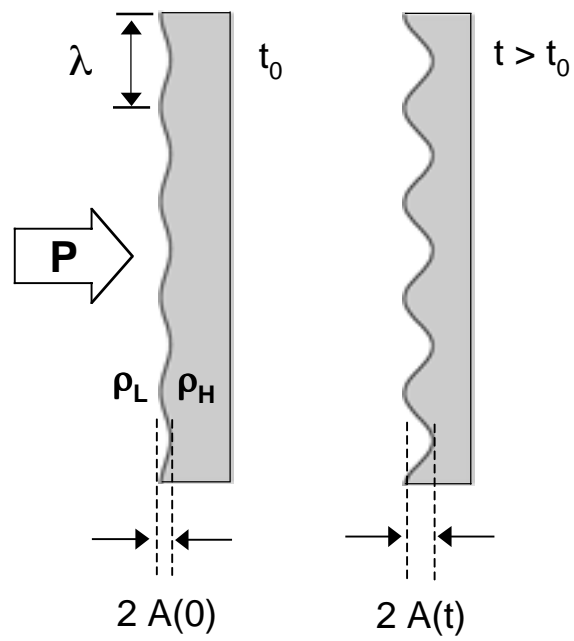
Lawrence Livermore National Laboratory
Livermore, CA

Abstract: A new approach to the study of material strength of metals at extreme pressures has been developed on the Omega laser, using a ramped plasma piston drive. The laser drives a shock through a solid plastic reservoir that unloads at the rear free surface, expands across a vacuum gap, and stagnates on the metal sample under study. This produces a gently increasing ram pressure, compressing the sample nearly isentropically. The peak pressure on the sample, inferred from VISAR measurements of velocity, can be varied by adjusting the laser energy and pulse length, gap size, and reservoir density, and obeys a simple scaling relation.¹ In an important application, using in-flight x-ray radiography, the material strength of solid-state samples at high pressure can be inferred by measuring the reductions in the growth rates (stabilization) of Rayleigh-Taylor (RT) unstable interfaces. This paper reports the first attempt to use this new laser-driven, quasi-isentropic technique for determining material strength in high-pressure solids. Modulated foils of Al-6061-T6 were accelerated and compressed to peak pressures of 200 kbar. Modulation growth was recorded at a series of times after peak acceleration and well into the release phase. Fits to the growth data, using a Steinberg-Guinan (SG) constitutive strength model², give yield strengths 30% greater than those given by the nominal parameters for Al-6061-T6. Calculations indicate that the dynamic enhancement to the yield strength at 200 kbar is a factor of $\sim 2.5\times$ over the ambient yield strength of 2.9 kbar. Experimental designs based on this drive developed for the NIF laser, predict that solid-state samples can be quasi-isentropically driven to pressures an order of magnitude higher than on Omega - accessing new regimes of dense, high-pressure matter.

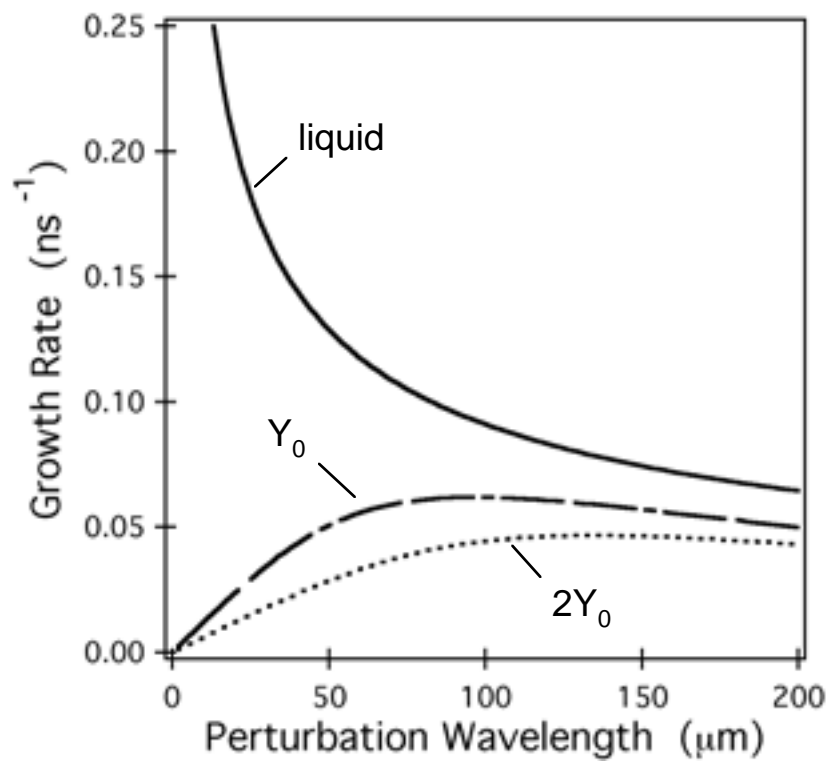


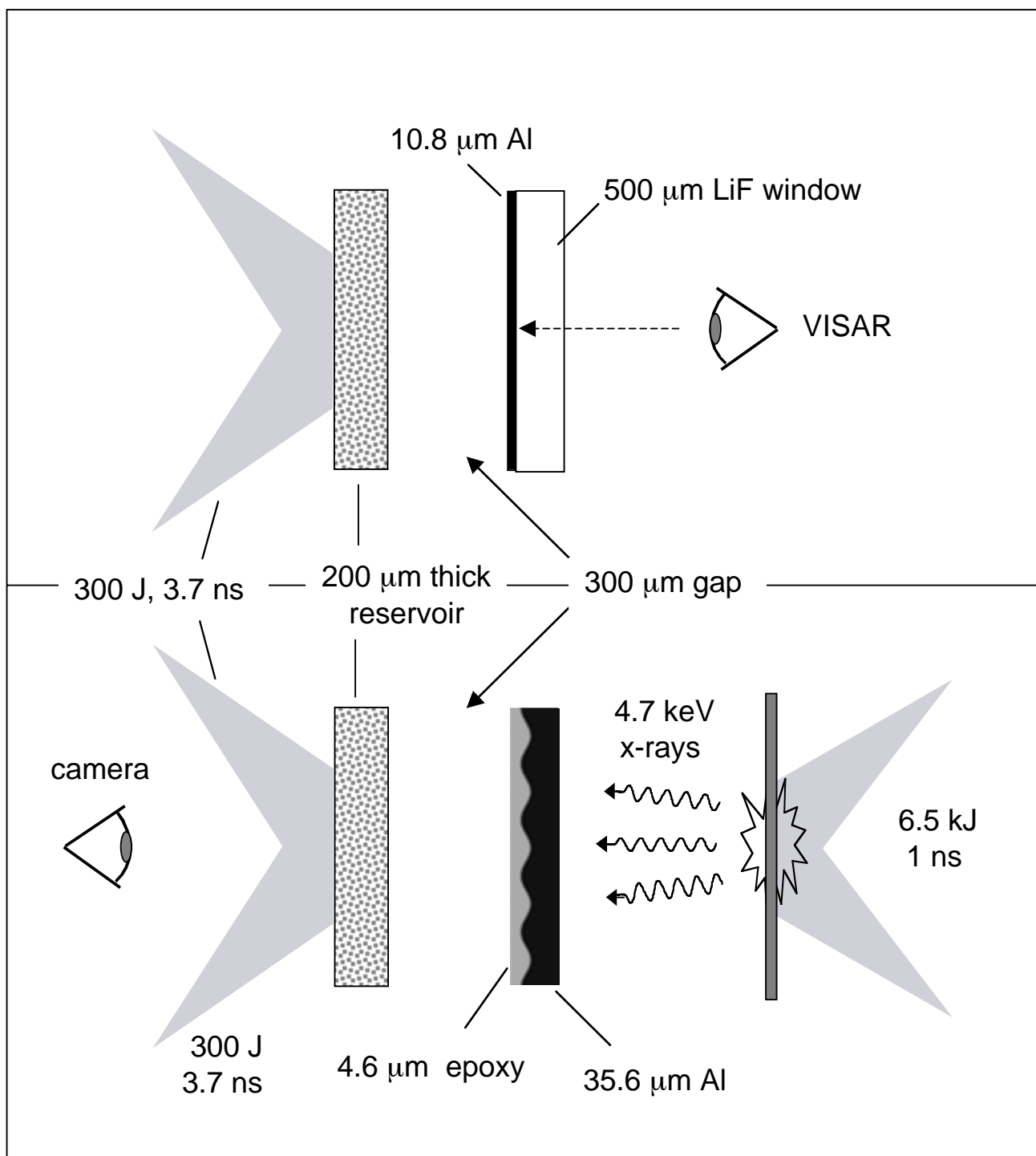
Lorenz_Figure_1

(a)



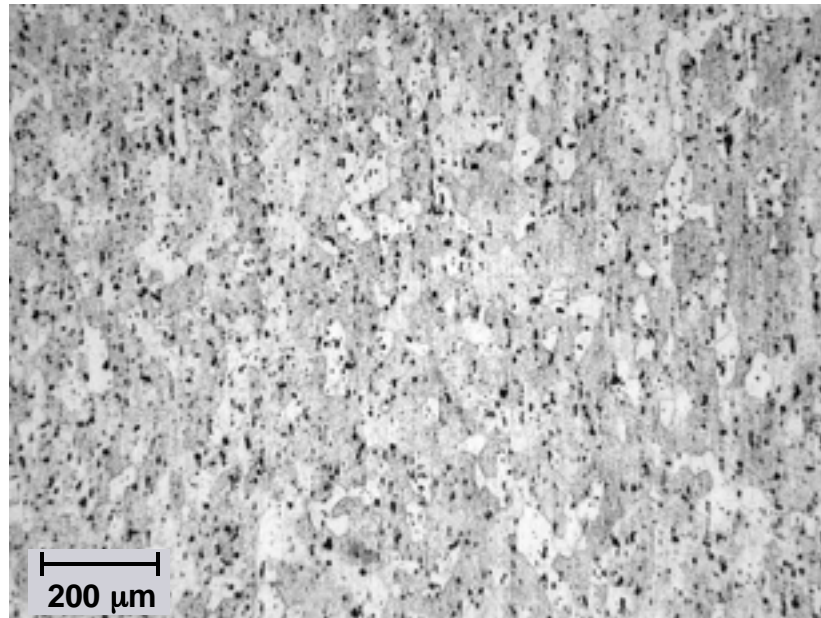
(b)



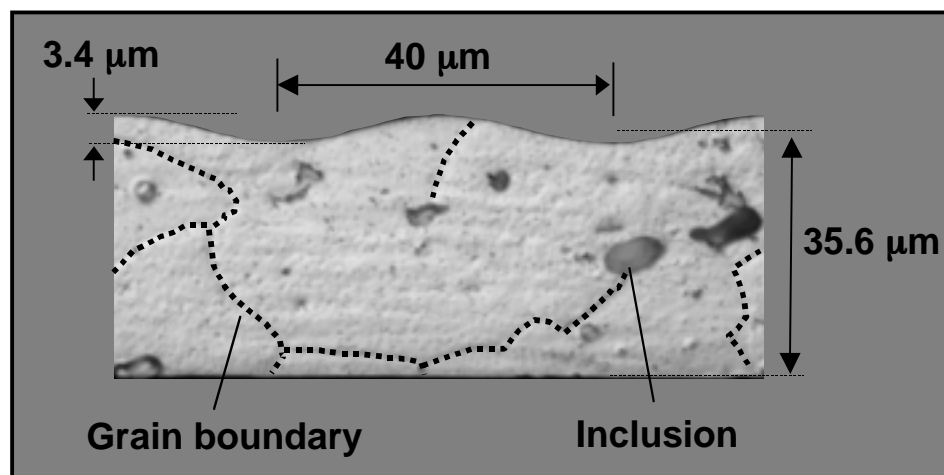


Lorenz_Figure_3

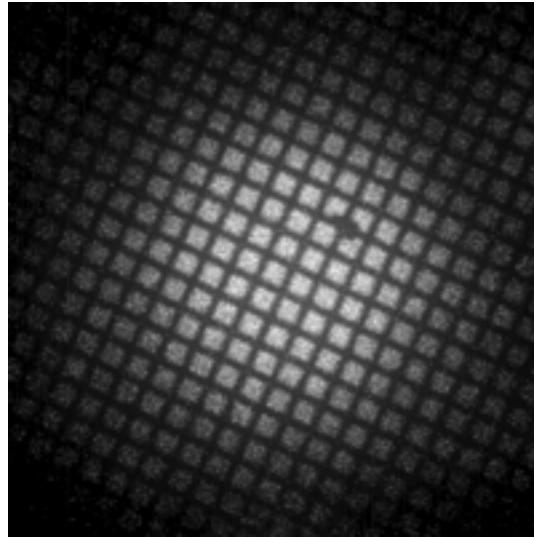
(a)



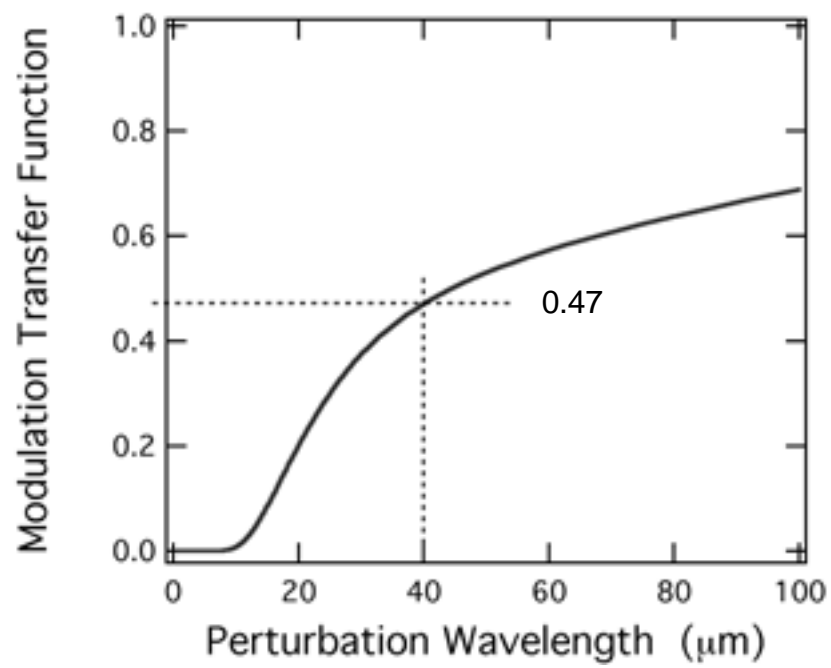
(b)



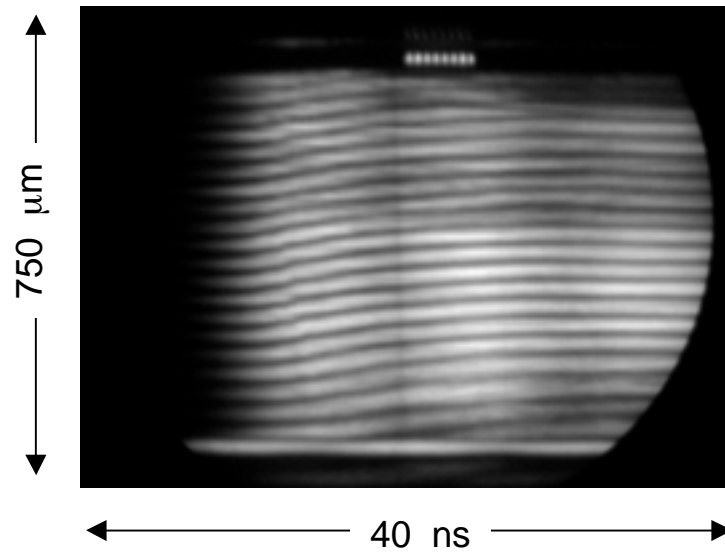
(a)



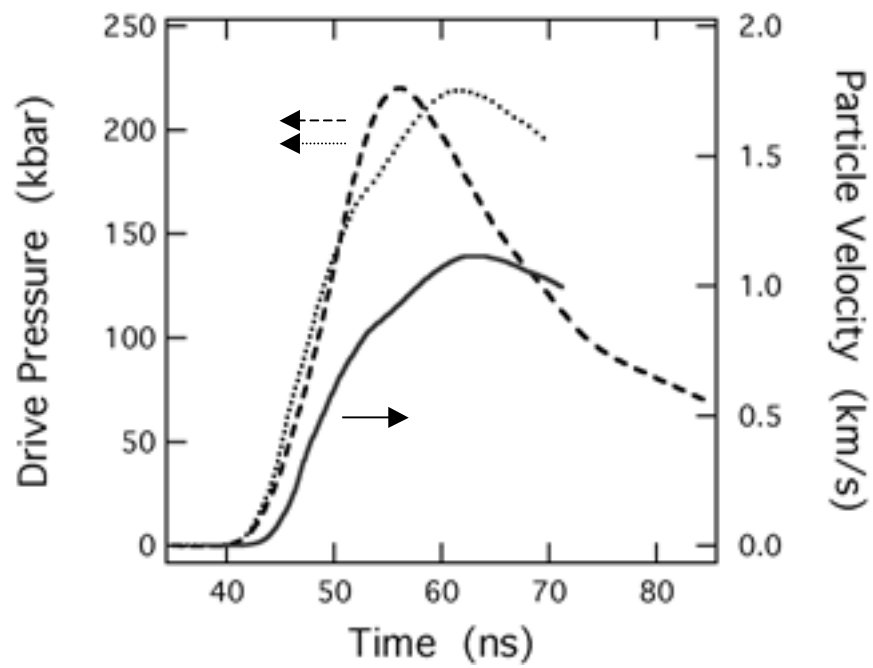
(b)

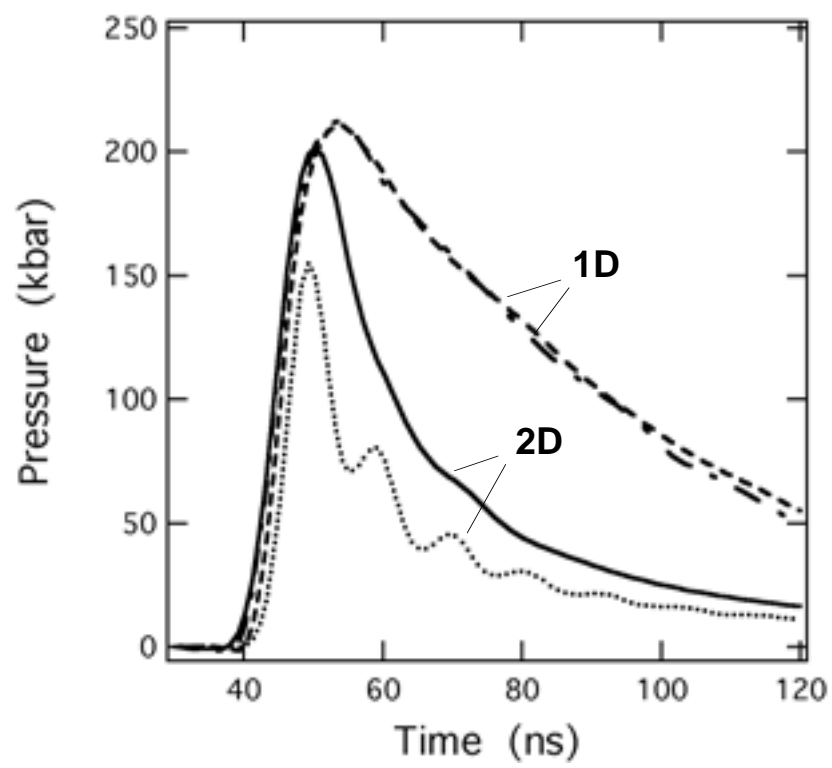


(a)



(b)



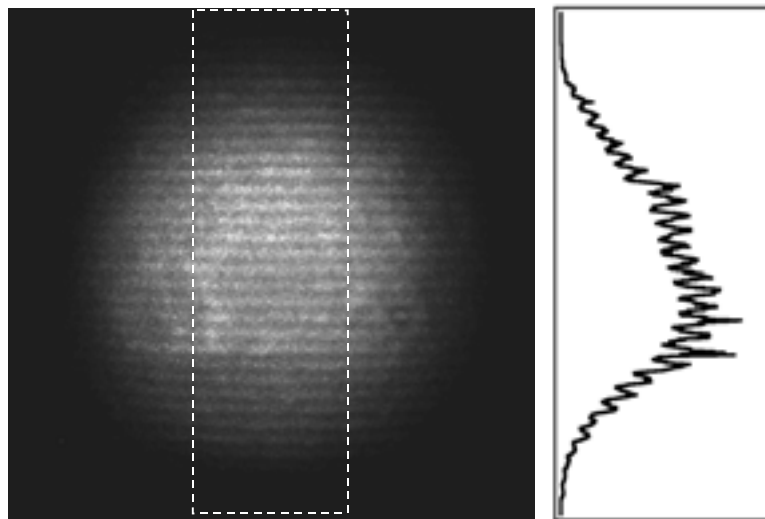


Lorenz_Figure_7

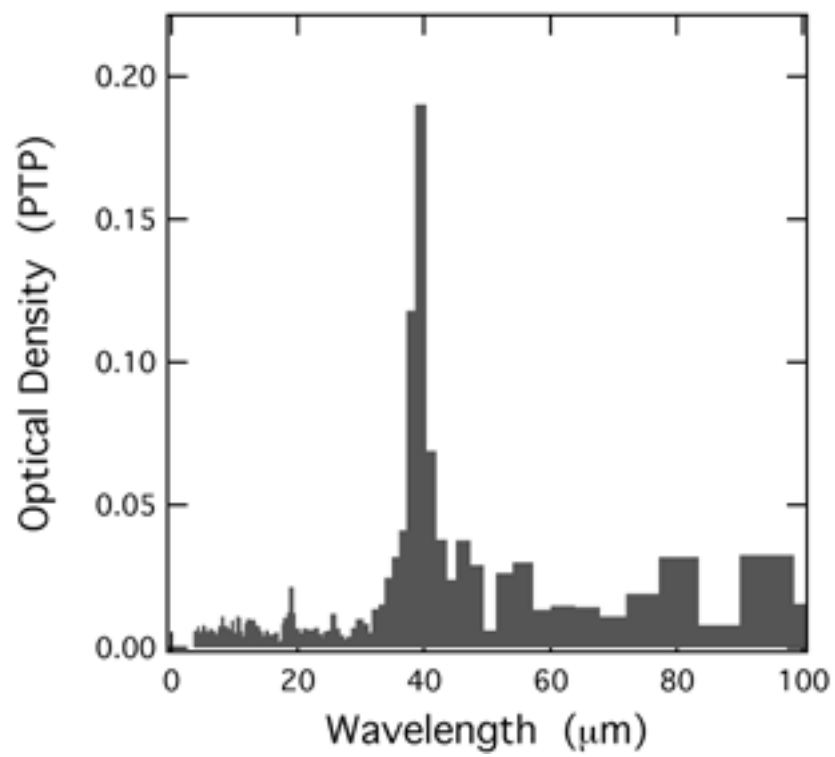
Table 1

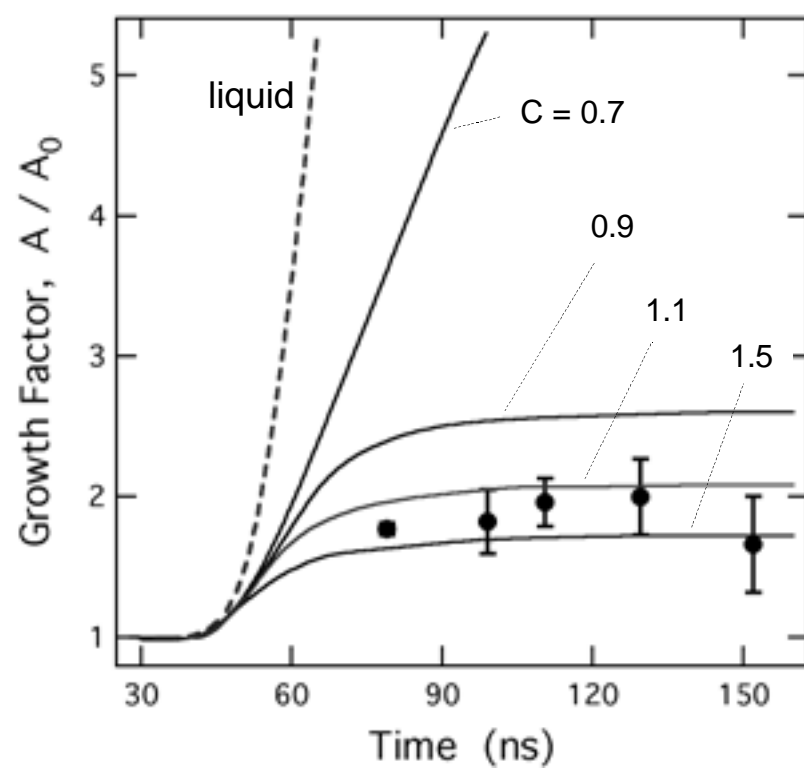
Shot	Laser Energy (J)	Reservoir (μm)	Gap (μm)	Pressure (kbar)	Radiograph Time (ns)	GF [A_{max} / A_0]
^a 37007	292.2	^c 208	335	220	-	-
^a 37008	296.4	^c 208	335	218	-	-
^b 37010	319.2	205	335	198	80	^d 1.77 ± 0.042
^b 37012	328.8	210	335	192	100	^d 1.82 ± 0.23
^b 37015	321.0	218	300	209	110	^e 1.96 ± 0.17
^b 37016	325.8	206	300	218	150	^e 1.66 ± 0.34
^b 37019	324.0	213	300	214	130	^e 2.00 ± 0.27

(a)

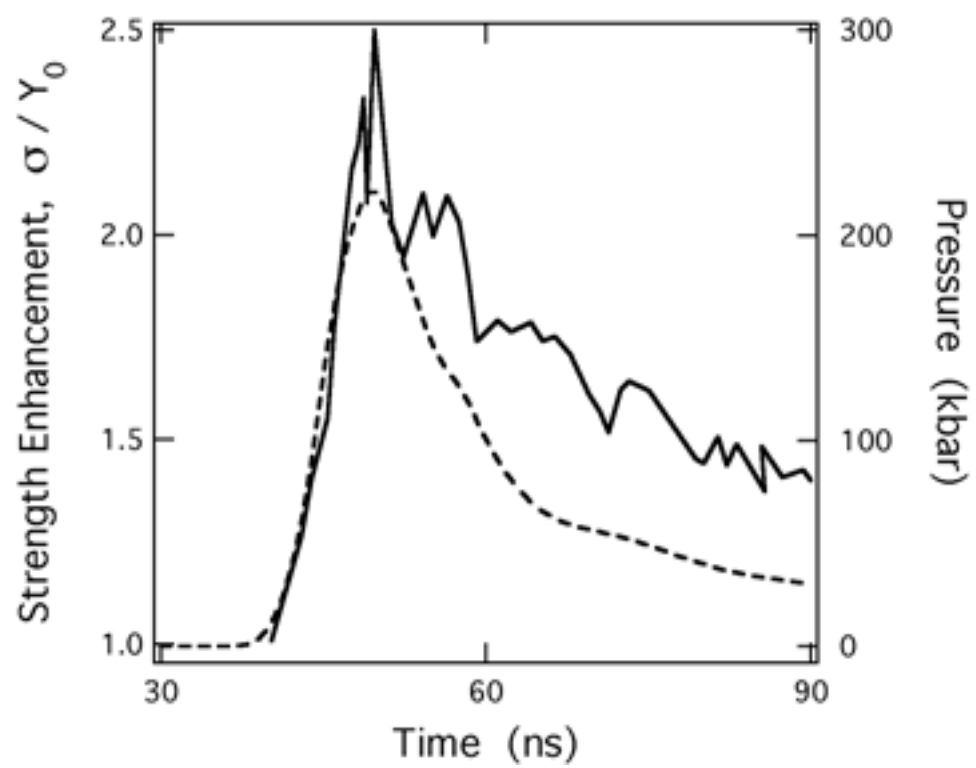


(b)





Lorenz_Figure_9



Lorenz_Figure_10

I. INTRODUCTION

The Earth's core is composed of iron and iron compounds. Temperatures at the inner core are above 5000 K.³ This temperature is high enough to melt iron in the lab. However, the Earth's inner core is solid. At the inner core boundary, the accumulated gravitational "weight" of the surrounding material adds up to pressures in excess of 3 million atmospheres. Saturn's core is at a pressure of more than 10 million atmospheres (10 Mbar or 1000 GPa).⁴ In terms of energy density, 10 Mbar is equivalent to 1 MJ/cm³ – enough energy density to turn unconstrained material to plasma. These ultrahigh pressure, high-energy-density states were formed by quasi-isentropic (gravitational) compression to create matter that is energetic, highly compressed and relatively "cold". Little is known about the behavior of matter under these unusual conditions, because planetary cores are difficult to access directly, and experimental techniques for reproducing these conditions in a controlled laboratory environment are largely unavailable. Of the various material properties that could be explored, our group is pursuing an effort to address a fundamental question: How does ultrahigh pressure affect material strength?

Strength is a material's resistance to deformation. Concrete, a common building material, has a tensile strength of ~600 p.s.i. (pounds per square inch). Wood and steel, two other common building materials, fail under tension at pressures of ~15000 and ~300,000 p.s.i., respectively. Different materials exhibit enormous differences in strength. The manner of loading on the material can make a difference. Concrete has ten times more compressive strength than tensile strength, whereas wood tends to be stronger in tension than compression. Part of the reason is that the deformation mechanisms are different under various loading conditions. Metals tend to fail from shearing in both compression and tension, and a material's resistance to shear forces characterizes its strength. Typically, the strength of a metal is characterized by its "yield point" – the stress at the onset of irreversible plastic deformation, and an accompanying flow rule, which describes the continued plastic deformation as a function of the material's stress-strain state. The flow rule for the yield strength of a metal varies with loading conditions, and is commonly described by a constitutive model,

$$\text{Yield strength, } Y = f(P, T, \varepsilon, \dot{\varepsilon}, \eta, S) \quad (1a)$$

where, P is pressure, T is temperature, ε is strain, $\dot{\varepsilon}$ is strain rate, η is compression, and S is a structure factor that depends on many different small-scale structural features that effect the strength – defects, alloying particles, etc. In general, increases in pressure, strain, strain rate, compression and number of defects will all increase the strength of a metal. Elevated temperature, on the other hand, will generally soften the material. In this paper we are examining the strength of Al-6061-T6 at a peak pressure of 200 kbar. Al-6061-T6 is a precipitation-hardened alloy of aluminum containing fine particles of Mg_2Si that

serve to inhibit plastic flow and thus strengthen the material. The Steinberg-Guinan (SG) constitutive model² suggests that Al-6061-T6 exhibits very strong pressure hardening behavior, that is, its strength is predicted to increase rapidly with pressure. For example, the strength of Al should increase by $\sim 7\times$ for every Mbar rise in pressure. At 10 Mbar, the its yield strength would be around 200 kbar, nearly two orders of magnitude above its ambient value!

Generating these pressures in Al will require a special type of driver. Figure 1 shows a P-T phase diagram for aluminum. The dashed line is the liquid-solid boundary, defined by a Lindemann² melt law. Notice that as you increase the pressure, the melt temperature rises as well. There are a number of paths to high-pressure solid states in aluminum. If one shocks the material, the sample is placed in a state that lies on the Hugoniot. The shock melting pressure for aluminum is ~ 1.2 Mbar, and defines the highest pressure attainable in the solid state under single-shock conditions. By using a series of smaller shocks, higher solid-state pressures can be reached. A path can be conceived that consists of an infinite series of very small shocks. In this way, one can approach the limit of compressing a material isentropically. We have developed a quasi-isentropic driver that uses a laser to create a “plasma piston” that can gently compress and accelerate metal foils without shocks.¹ Material strength is inferred using a technique of inducing a Rayleigh-Taylor (RT) instability in the foil while under load, and measuring the growth of the instabilities using in-flight x-ray radiography.

The remainder of the paper is organized as follows: II) An explanation of the RT strength technique and the plasma-piston driver, III) Characterization of our camera imaging system, IV) Characterization of the drive, V) Experimental Results, VI) Discussion and VII) Summary.

II. EXPERIMENTAL TECHNIQUE

A. Material Strength using the Rayleigh-Taylor Instability

Dynamic material strength at high pressures can be evaluated using the technique of Rayleigh-Taylor (RT) hydrodynamic instabilities in solid plates.⁵⁻¹⁰ A metal sample is accelerated by a lower density, high-pressure “pusher”, creating a situation where the interface between sample and pusher is hydrodynamically unstable. Any preexisting perturbations at the interface will attempt to grow. Material strength in the sample will inhibit or slow the growth of the fluid-solid instability relative to a fluid-fluid instability. Figure 2a shows the situation schematically. Our technique here closely follows the early work of Barnes.⁵ In those experiments, the detonation products from a high explosive slab – offset from the sample by a vacuum gap, smoothly accelerate and compress the plate. Precut modulations on the driven side of the plate grow over time. The growth rate increases with drive pressure, but is reduced and stabilized by material strength, increased plate thickness and smaller initial modulation amplitudes, A_0 .

In classical fluid RT instability growth (for incompressible, inviscid fluids), the growth rate increases without bound as the wavelength, λ , decreases. The growth rate, γ , of the interface is simply $\gamma^2 = Akg$, where $A = (\rho_H - \rho_L)/(\rho_H + \rho_L)$ is the Atwood number, $k = 2\pi/\lambda$ is the perturbation wavenumber, and g is the acceleration. The time-dependent growth for a perturbation having an initial amplitude, δA_0 is given by $\delta A(t) = \delta A_0 e^{\gamma t}$. In real fluids, viscosity (ν) and surface tension can reduce the growth or even stabilize the RT evolution. In this situation, an interface may be stabilized if its perturbation wavelength and amplitude fall below some critical value [ref]. An analogous analytical solution exists for a plate of thickness (h), under uniform acceleration, g .^{11,12} The surface tension is replaced by the shear modulus (G) of the material and the solid “flow” is moderated by an effective lattice viscosity, $\nu_{\text{eff}} = \sigma/(6^{1/2}\rho(d\varepsilon/dt))$, where σ is the material strength. This leads to a RT dispersion curve of the form

$$\gamma^2 + 2k^2\nu_{\text{eff}}\gamma + k \tanh(kh) \left(\frac{kG}{\rho} - Ag \right) = 0, \quad (2)$$

where γ is the RT growth rate for the fluid-solid interface. This has the solution

$$\gamma = \nu_{\text{eff}} k^2 \left(\left(1 - \left(\frac{C}{\nu_{\text{eff}}^2 k^3} \right) \right)^{1/2} - 1 \right), \quad (3)$$

where $C = \tanh(kh)(kG/\rho - Ag)$. For incompressible inviscid fluids (no material strength), where $\nu_{\text{eff}} = 0$ and $G = 0$, the classical result, $\gamma^2 = Akg$, is recovered. For solids in the elastic regime, ν_{eff} is still zero, but G is finite and perturbation growth is reversible. Beyond the elastic limit, material begins to flow plastically. In this regime, $G = 0$ and plastic flow is regulated by the effective lattice viscosity. The plastic flow is reduced by high material strength (σ), which acts as an effective lattice viscosity, but high strain rate ($d\varepsilon/dt$) increases RT growth by lowering the effective viscosity.

The effect of perturbation wavelength is shown graphically in Fig. 2b for an Al-6061-T6 sample. The growth rates assume a 36 μm thick sample foil driven at a pressure of 200 kbar. (This is the peak design pressure for the strength experiments presented in this paper.) Values for the shear modulus, $G = 27.6$ GPa, and initial yield strength, $Y_0 = 0.29$ GPa, are taken from Steinberg.² The “liquid” case represents an Al-6061-T6 foil with no shear strength, or $Y = 0$. The liquid RT growth rate at peak pressure is many times that of the solid at short wavelengths. At long perturbation wavelengths the solid starts exhibiting fluid-like behavior. The solid RT growth is reduced from that of the liquid due to material strength, but also exhibits a maximum growth wavelength, depending on the shear strength. Stronger material, for a given density, acceleration and foil thickness, reduces the growth still further and shifts the maximum growth rate

towards longer perturbation wavelengths. An ideal RT strength experiment has strong strength effects compared to a liquid, especially at shorter wavelengths. However, the perturbation wavelengths cannot be at a scale length shorter than the spatial resolution of the experimental imaging diagnostic. This lower resolution limit, which is partially driven by signal-to-noise criteria, is about 20 microns using the techniques and diagnostics used in this paper. (Other imaging techniques offer better resolution and S/N.¹³) A second sensitivity issue arises when designing an RT strength experiment. If the overall RT growth is too large, the perturbations will enter the non-linear regime. Diagnosis and analysis of the nonlinear bubble and spike structures may become difficult. On the other hand, if the growth rate is very small, then there may be insufficient differences between the “peaks” and “valleys” of the perturbation to experimentally resolve. This experiment was designed with a perturbation wavelength of 40 μm , placing it in a comfortable regime having sufficient strength stabilization and of long enough spatial scale to resolve with our imaging system.

The above analysis assumes that acceleration is a constant and is uniform throughout the sample. In practice, a thin plate is accelerated by a time-dependent, drive pressure on one surface, while the opposite surface resides at ambient pressure. This sets up a situation where the body is subjected to temporal and spatial stress gradients, and where compression and release waves propagate back and forth throughout the plate.¹⁴ Therefore, simple analytical formulas can only give qualitative behavior and detailed pre-shot design and post-shot analysis must use numerical methods. For this we use a two-dimensional (2D) radiation-hydrodynamics code (LASNEX)¹⁵ along with the SG constitutive strength model to simulate RT growth in our samples.

B. The Plasma-Piston Driver

The pressure source for the RT strength experiments must satisfy two conditions. First, it must compress and accelerate the sample without strong shocks. The absence of a strong shock will keep temperatures below the melt temperature at high pressures. Second, the pressure source needs to establish an RT instability at the front face of the sample. The detonation products produced in Barnes’ early RT strength work were low-density, gaseous species. The Atwood number at the perturbation surface is approximately $A \sim 1$ as the HE products arrive. As they compress against the sample, the value of A decreases, but not nearly enough to modify the RT growth.

We have developed a shockless driver modeled on Barnes’ technique using a laser as the energy source.¹ Figure 3 shows a schematic diagram of our target and experimental geometry. We replace the HE slab with a thin slab of plastic (reservoir) that serves as the material for the low-density pusher. The reservoir is “energized” by depositing a high-energy pulse of light onto the front face of the plastic. A strong ablative shock is generated at the front face and propagates through the reservoir to the rear surface. At this point, the reservoir

unloads and expands into a vacuum gap as gaseous “ejecta”. The reservoir gas expands across the vacuum gap – generating a smoothly decreasing density distribution from the reservoir to the sample. The pressure applied to the sample is the ram pressure, $P_{ram} = \rho_{ejecta} u_{ejecta}^2$, of the inflowing ejecta, which increases smoothly and monotonically in time as the reservoir unloads. The rarefaction wave from the front side of the reservoir (where the laser was incident) eventually releases the remaining reservoir pressure, and the peak pressure in the sample starts to decrease.

Two target variations are used in this experiment. The first variation, shown at the top of Fig. 3, uses a surrogate aluminum-LiF sample to calibrate the drive for the RT strength experiments. This target is made by electron-beam vapor deposition of aluminum onto a LiF substrate. The substrate temperature during the deposition process was monitored carefully to ensure that the aluminum was deposited at full density. The density of the aluminum film was measured to be 2.70 gm/cm^3 – that of fully dense polycrystalline aluminum. The Al-LiF sample is positioned at a distance equivalent to the RT target gap spacing. The compression wave from the unloading reservoir propagates through the Al layer and into the LiF window. The Al and LiF are very nearly impedance matched, eliminating nearly all reflected waves at the Al-LiF interface. A VISAR¹⁶ records the motion of the Al-LiF interface. This is the in-situ particle velocity of the compression wave as it leaves the Al. Using the recorded particle velocity, along with the known equation-of-state (EOS) of the aluminum, a “back-integration” analysis technique^{17,18} will generate the time-dependent pressure, $P(t)$, that was applied to the front face of the sample. We use $P(t)$ as our known drive in modeling the RT strength results.

For the RT strength experiments, the Al-LiF surrogate is replaced with a RT target having modulations cut into the driven surface (facing reservoir). A thin layer of thermal plastic or epoxy was applied to machined perturbation surface to insulate it from thermal loading of the incoming reservoir material as it stagnates against the sample surface. The epoxy used for the thermal shield has a yield strength of 0.165 kbar at room temperature and pressure, which is less than 6% the strength of the Al-6061-T6 sample. At temperatures as low as 400 K, the epoxy strength falls by a factor of 5, and is not considered to affect the determination of the dynamic strength of the aluminum sample. To record the growth of the perturbations, a 4.7 keV x-ray source is generated using sixteen beams (1 ns) totaling ~6.5 kJ energy at 355 nm deposited onto a 10 μm thick Ti foil in an 800 μm spot (fwhm). These x-rays penetrate the foil in-flight and are recorded in a gated x-ray pinhole camera^{19,20}, capturing a snapshot of the rippled foil as it accelerates away from its original position. The image produced captures the differential absorption (contrast) between the thicker peaks and thinner valleys of the valley (see Fig. 2a). Each laser shot records the RT growth for a single time during the evolution of the RT instability growth. A series of laser shots – ideally generating exactly the same drive conditions, maps out the time-dependent RT growth in the sample. This growth is then modeled using a

constitutive strength model to infer the dynamic strength of the sample material under the measured drive conditions.

C. RT Sample Preparation

The material used in this study was a common aluminum alloy, Al6061 in the T6 condition, purchased in the form of a 4.82 mm thick plate. Standard metallographic techniques, looking at three perpendicular sections through the plate, were used to determine a grain size of approximately 38 μm and that the grain morphology was roughly equiaxed. Additional examination using electron backscatter diffraction revealed a randomly oriented crystallite distribution. Figure 4a, taken of a polished and etched surface, shows the general microstructure of this material. The primary alloying elements are Mg and Si with smaller additions of Cu and Fe. This alloy derives its strength through precipitation of the alloying elements during heat treatment. These precipitates (Mg_2Si) are on a very fine (50-250 nm) scale and act as obstacles to dislocation motion, increasing the material strength. In addition to these fine precipitates there are many larger second phase regions primarily Mg_2Si and AlFeSi , which appear as small dark regions in figure Fig 4a. These particles, which are too big and widely spaced to act as effective obstacles to dislocation motion, nonetheless may affect the overall plastic flow patterns in the material and material failure characteristics. These particles may in themselves serve as sites for RT instabilities and generate failure zones in high strain regimes.

Samples for the RT experiments were machined from ~5 mm thick plate stock material. Successive machining operations, using single point diamond turning, were used to reduce the plate thickness to ~200 μm . Subsequent thinning, to achieve the final sample thickness, was done in only a small region. Finally, a sinusoidal pattern was cut in a single machining pass to provide the desired initial amplitude and frequency for subsequent RT growth. Figure 4b shows a cross-sectioned image of a test sample from the batch of targets used in this study. The large particles, called inclusions, were discussed above. A few grains have been outlined for easy visibility. Mean sample thickness is 35.6 μm . The peak-to-peak (PTP) perturbation amplitude is 3.4 μm and the perturbation wavelength is 40 μm .

III. DETERMINATION OF THE CAMERA RESOLUTION FUNCTION

RT growth in the driven samples is measured by face-on radiography, where the line-of-sight is normal to the sample surface. The RT instability features show up as alternating bright and dim lines – representing x-ray transmission through the thinner valleys and thicker peaks, respectively. The relative intensity (contrast) between the peaks and valleys is directly related to the perturbation amplitude. Equivalently, the difference in optical depth, $\delta\text{OD} =$

$\Delta \ln(\text{intensity})$, where $\delta OD(t) = A(t)/MFP$, where $A(t)$ is the perturbation amplitude, and MFP is the mean free path or thickness where the x-ray signal falls to $1/e$ its original intensity. The ability of the camera system to accurately reproduce the contrast in the sample is given by the modulation transfer function (MTF), namely, the ratio of observed to actual contrast. The MTF is generally plotted as a function of spatial wavelength and depends for the most part on the pinhole diameter in pinhole imaging systems.

The imaging system consisted of a 2×2 pinhole array which projects four images onto a microchannel plate (MCP) image intensifier, which is coupled to either film or a CCD *via* a fiber bundle array. All experimental shots produced four “equivalent” images. Small differences are due mainly to differences in the size and shape of the four individual pinholes. We have characterized our MTF by imaging an undriven, gold SEM grid. The grid spacing was $63.5 \mu\text{m}$ between wire centers, while the wires were $\sim 21 \mu\text{m}$ thick. Figure 5a shows a radiographic image of the SEM grid. This image was simulated assuming a resolution function consisting of the sum of a gaussian and an exponential tail²¹

$$R(x) = \frac{1}{1 + \alpha} \left(e^{\frac{-x^2}{\sigma^2}} + \alpha e^{\frac{-x}{\tau}} \right) \quad (4)$$

where α , σ and τ are adjustable parameters of a fit. The fit parameters were determined from a best fit of the convolution of an ideal grid with the resolution function $R(x)$ to the measured grid image. Best fit parameters for α , σ and τ are 9.0 , $0.046 \mu\text{m}$ and $25.1 \mu\text{m}$, respectively. The MTF is the Fourier transform of the resolution function, $R(x)$. An average MTF for the individual pinholes was determined and is shown in Fig. 5b. A value of 0.47 ± 0.03 was determined for the perturbation wavelength of $40 \mu\text{m}$. Given this, the measured RT perturbation growth can be expressed as a growth factor (GF) which is the ratio of the perturbation amplitude at the measured time to the initial perturbation amplitude: $GF(t) = A(t)/A_0$. Expressing this in optical density,

$$\text{growth factor, } GF(t) = \frac{\delta OD(t)}{\left(\frac{A_0}{MFP} \right) MTF} \quad (5)$$

where $A_0 = 3.4 \mu\text{m}$, $MFP = 16.8 \mu\text{m}$, $MTF = 0.47$ and $\delta OD = \Delta \ln(\text{intensity})$. This last value is determined using the PTP (peak-to-peak) value for a wave modulation in a lineout across an experimental image of the driven RT foil. Details on our method for extracting GF's of driven foils follows below.

IV. DETERMINATION OF THE DRIVE

The measured quantity from which we are determining the material strength is the time-dependent RT growth of the foil perturbations. Strength is inferred by hydrodynamically simulating the entire mass flow in the target, beginning with the laser ablation of the reservoir. A constitutive strength model is included in the hydro-code, which moderates the RT growth in the sample in accordance with the other known parameters of the experiment and constrained by the RT growth data. The pressure in the target and the gross foil trajectory can be calibrated using a surrogate target and a line VISAR to diagnose the particle velocity of the accelerating sample (see Fig. 3).

Drive calibration shots were performed on Al-LiF samples. A 10.76 μm layer of Al was applied to a 500 μm thick LiF optical flat. The Al-LiF sample was assembled together with a composite reservoir consisting of – in order from laser ablation side toward the gap, 0.05 nm Al coating, 165 μm polycarbonate ($\text{C}_4\text{H}_4\text{O}$, $\rho = 1.2 \text{ g/cm}^3$) and 35 μm of 2 atomic percent brominated polystyrene ($\text{C}_{50}\text{H}_{48}\text{Br}_2$, $\rho = 1.2 \text{ g/cm}^3$), along with a spacer to create the necessary vacuum gap between reservoir and sample. Six laser beams totaling approximately 300 J were focused onto the front face of the reservoir using phase plates to shape the beam spot profile. The on-target profile for the six overlapped beams can be described by a superGaussian,

$$I(r) = I_0 e^{-\left(\frac{r^2}{530 \mu\text{m}}\right)^4}, \quad (6)$$

which puts approximately 35% of the total beam energy into a circle 600 μm in diameter, with intensity greater than 90% of the maximum intensity, of $\sim 1.0 \times 10^{13} \text{ W/cm}^2$ across the central portion of the drive region. The pulse duration was a 3.7 ns square pulse using the third harmonic at a wavelength of 351 nm (3ω).

Figure 6a shows a typical VISAR record used for drive calibration. The VISAR records fringe displacement as a function of time (horizontal axis) and position on the target (vertical axis). Fringe motion tracks the velocity of the reflective Al-LiF interface – in this case it is the particle velocity of the aluminum at the interface. For this record, the “window-corrected” fringe spacing was 640 m/s per fringe. Note the smooth acceleration up to a maximum velocity of about 1.1 km/s. Figure 6b shows a plot of the extracted particle velocity vs time from this shot (solid line). The loading history at the front surface of the sample has been extracted by a “back-integration” technique^{17,18} from the particle velocity trace. Using the known EOS for Al and the Al layer thickness, the standard Euler equations were integrated backward in space to the front of the sample, using the experimental particle velocity as the initial condition. The resulting pressure profile is shown in Fig. 6b as a dotted line. The VISAR has a time window currently limited to about 35 ns. The dashed line shows a LASNEX¹⁵ hydrocode simulation of the drive pressure at the front of the sample. The simulation shows good agreement with the peak pressure and the early stages of the compression, but disagrees slightly with some of the detailed structure near peak pressure. We

do not expect the experimental results to be particularly sensitive to this level of discrepancy. The detailed parameters for the set of shots presented in this paper are listed in Table 1. The table lists two drive calibration shots that were closely matched in laser energy and in the resulting extracted pressure profiles. Each shot was simulated using the hydrocode, including differences in individual target dimensions. The experimental RT growth results were then normalized for differences in drive pressure. Peak pressures for each shot are also listed in Table 1.

Figure 7 shows both 1D and 2D LASNEX calculations of the applied pressure to a flat variant of the RT samples. The sample consists of 4.6 μm epoxy ($\text{C}_{5.66}\text{H}_{7.33}\text{N}_{0.3}\text{O}$, $\rho = 1.185 \text{ g/cm}^3$) followed by 35.6 μm Al – with no perturbation on the Al. These calculations were done for a peak pressure that was an average of all the experimental RT shots. The two upper curves are 1D calculations of $P(t)$ at the front of the sample (dot-dash) and 5 μm into the sample (dash). They are essentially identical to one another. The two lower curves show 2D calculations for the same drive conditions. Note that the peak pressure is slightly lower, but the late-time pressure profile is dramatically different. This is due to 2D release effects inside the sample, which are not captured in the 1D calculations. Note also that the 2D calculations capture some of the more complex wave dynamics inside the target. The solid line shows $P(t)$ at the front face, while the dotted line shows $P(t)$ at 5 μm inside the sample. The peak pressure is reduced and the pressure profile shows undulations in time. The compression effects inside a thin foil are complex. The foot of the forward moving compression wave will reflect from the rear surface of the sample, reverse direction, and overlap with the still-evolving forward wave. In fact, the material may be subjected to many waves propagating back and forth between the front and rear surfaces of the foil. Swegle and Robinson have dealt with this topic in detail.¹⁴ Full 2D numerical modeling is required to capture the detailed hydrodynamics in these experiments.

V. RESULTS AND ANALYSIS OF RT GROWTH

RT growth data in Al-6061-T6 was acquired at five points in time during the acceleration and coast portions of the foil's trajectory. Times were chosen based on pre-shot estimates of growth for the expected pressure profiles. During the early stages of RT growth, it can be difficult to discriminate fluid-like behavior from RT behavior exhibiting strength effects. Even though the growth rate is higher in the fluid case, the integrated perturbation growth for both the fluid case (no strength) and the solid case (strength), may be too low to differentiate the two cases. In materials that exhibit significant strength stabilization, the RT growth asymptotes at late time when the drive pressure starts to decrease, whereas the fluid cases maintain their high rate of growth. Data acquisition at times after the pressure peak are desirable as long as the growth has not moved significantly into the non-linear regime, where the peaks will form spikes and then begin to roll

up. In this experiment, the drive peaked at 200 kbar at the front face of the sample at 50 ns after the drive laser turned on. Measurable growth was not expected for another 20-30 ns, so we began our acquisition times at $t_0 + 80$ ns. Table 1 lists the specifics for the five RT shots as well as the timing for those shots. Note also, that shots 37010 and 37012 were recorded on CCD while the remaining shots were recorded on optical film (see section III above). These optical film images required additional corrections for film response.

Figure 8a shows an in-flight radiograph from shot 37019. For presentation purposes, the radiograph shown is an image that was built up from the four individual radiographs that are acquired on each shot – these four images are those that are projected through a 2x2 pinhole array on the front of the x-ray imaging camera. The peaks (dark lines) and valleys (bright lines) can be clearly seen. The field-of-view for this image is about 1.4x1.4 mm on the target. A lineout is shown to the right of the image. This lineout has both the intensity modulation pattern associated with differential transmission through adjacent peaks and valleys, but also includes the spatial intensity profile from the x-ray source, which is about 800 μm (fwhm) across. This source profile is fit and subtracted from the lineout resulting in a spatially dependent modulation centered about zero. For each shot, all four individual data images were analyzed, using lineouts that were averaged over 400 μm . A 400 μm wide box is drawn over the radiograph (dashed line) shown in Fig 8a.

The differential optical density, δOD , can be determined by taking the Fourier transform of the $\ln(\text{lineout intensity})$, giving the δOD as a function of wavelength. Figure 8b shows a plot of δOD versus wavelength for the radiograph shown in (a). The value for 40 μm mode is then substituted into Eq. (5) to determine the perturbation growth factor. For this work, some of the data was acquired at high signal levels, and there was a significant variation in the exposure level across any single image. At high signal levels, gated MCPs are observed to enter the non-linear regime.^{22,23} Therefore the images were analyzed to determine the measured modulation as a function of exposure for each period in each image. The correlation between signal level and modulation was then examined. For periods with signal levels greater than 3000 counts (or a 0.4 ergs/cm² exposure on TMAX 3200 film), modulation amplitude showed a strong correlation with the signal intensity, suggesting an onset of non-linearity in the camera system. Periods with signal levels over 3000 counts or a 0.4 exposure level on film have not been included in our reported GF results.

Growth factors (GF) were calculated for variations in drive pressure and target specifications present in each shot. The measured GF at each time was normalized to the average target and drive conditions using the calculated GFs at that time. These experimental GFs are shown in Fig. 9. Measured GFs include error bars showing the standard deviation in the GF values over all individual periods analyzed for a given shot-time. Note that these GF's rise to a value a little below 2 at $t_0 + 80$ ns, with no significant growth over the next 70 ns. It appears that RT growth has stabilized with attenuation of pressure in the sample.

This contrasts RT growth behavior that is typical in fluids, where the instability continues to grow after the acceleration phase and into the coasting phase. This behavior is shown as a dotted line labeled “liquid”. This line is based on a calculation of an Al-6061-T6 target having zero material strength – as if it was melted. Compared to the overall growth shown for the liquid case, the Al data shows remarkable material strength stabilization.

The remaining lines, shown in Fig. 9, are GF(t) simulations for Al-6061-T6 having a range of inherent yield strengths. The calculated growth curves assume a SG yield strength model², given by

$$Y_{SG} = Y_0 \left[1 + \beta(\varepsilon_p + \varepsilon_i) \right]^n \left\{ 1 + A \frac{P}{\eta^{1/3}} - B(T - 300) \right\} \quad (7)$$

where Y_{SG} is the dynamic yield strength, Y_0 is the yield stress at RTP (room temperature and pressure) conditions, ε_p is the plastic strain, ε_i is any initial plastic strain before deformation begins, P is pressure, T is temperature, and η is volumetric compression. The variables β , n , A and B are fitting parameters having values 125, 0.1, 6.52 Mbar⁻¹ and 0.000616 K⁻¹, respectively. This flow strength model scales the dynamic strength to the RTP yield strength. The model includes strain hardening (terms enclosed in square brackets), pressure hardening (A-term) and thermal softening (B-term). All growth calculations assume average values for target and drive conditions from Table 1.

The dashed line indicates the calculated GF(t) in the sample using the nominal SG fitting parameters listed above. This growth curve over-predicts the amount of RT growth compared to the experimental data points. We can estimate the overall importance of the various model parameters before deciding how to fit the experimental data with a modified SG model. At early times, the dynamic strength is dominated by the pressure term, and at late times strain hardening becomes the dominant player. The estimated temperature in the foil ranges from 425 K on the isentrope to 490 K on the Hugoniot. The temperature must be between the two, but is likely much closer to the isentrope. A value of $T = 450$ K gives a temperature softening of -0.09 , a small effect. Using calculated LASNEX values for the compression, $\eta = 1.18$ at 200 kbar, the pressure hardening term is 1.23. An estimate of the gross shear strain can be derived from geometry and the experimental GFs, where the shear strain, $\varepsilon \sim 2A_0(GF-1)/(\lambda/2)$. At 50 ns, the calculated GFs appear to be between 1.1 and 1.3, giving values for the shear strain of 0.017-0.051. Using an average value of $\varepsilon_p \sim 0.034$, and assuming $\varepsilon_i = 0$, the estimated strain hardening term becomes 1.18. This is comparable to the pressure hardening. The limited amount of growth data presented here could not adequately constrain all the parameters in this model. Therefore, we have varied only the pressure-hardening term A , in order to fit the data. The solid lines in Fig. 9 show RT growth for a range of A -values; $0.7 \times A_{SG}$, $1.5 \times A_{SG}$, and $2.0 \times A_{SG}$, where $A_{SG} = 6.52$ Mbar⁻¹. The RT growth stabilizes at about 1.5-1.7 times A_{SG} . This corresponds to a dynamic strength, Y_{SG} , value

given by Eq. (7) that is ~30% greater than the value obtained using the nominal values for the fitting parameters listed above.

VI. DISCUSSION

The SG model assumes that material strength scales with shear modulus, and the shear modulus scales with pressure. This assumption would suggest that there is no upper bound to the strength if sufficient pressure is applied. While models suggest that pressure-scaling effects can vary from very weak to quite strong, Al-6061-T6 is expected to scale strongly with pressure. The SG pressure scaling term (A) for Al-6061-T6 is large, about 6.5 per Mbar. This means that the dynamic strength increases by a factor of 6.5 for every Mbar increase in applied pressure to the sample. The drive pressure in this experiment – 200 kbar, is nearly 70 times the yield strength of Al-6061-T6. This is not considered ultrahigh pressure for many current experimental techniques. Nonetheless, strength effects are not negligible at these pressure levels. An estimate of the strength effects at this pressure can be determined by comparing the dynamic strength at any time during the pressurization and deformation process to the RTP yield strength (Y_0).

Calculations tracked the strength throughout the sample volume as a function of time. For each time step, a weighted average of the strength was estimated by weighting the individual calculational cells in the target volume by the strain rate in that cell. In this way, the strength throughout the sample is weighted toward the regions where the most deformation is taking place at that time. Figure 10 shows the dynamic strength, Y_{SG}/Y_0 , as a function of time (solid line). The dashed line shows the applied pressure to the front face of the sample on the same time scale. The first thing to note is that the dynamic strength follows the pressure. This is not surprising, as the SG pressure parameter for Al-6061-T6 is large relative to the thermal softening or strain parameters. Note that the dynamic strength remains at about 1.4 at the 90 ns mark. At this point the pressure has dropped to just a few 10's of kbar. It is reasonable to assume that this is due to residual strain hardening in the sample material. Cold rolling or other forms of work hardening generate additional strength in a metal in a similar fashion – by generating large amounts of deformation or strain. This plot of the dynamic strength enhancement shows how the strength evolves along the entire deformation path.

This work is the first installment of a broad effort to study high-pressure, solid state properties, including strength. We have reported dynamic strength measurements of Al-6061-T6 driven to 200 kbar. The experimental design used 300 J of laser energy to load the sample quasi-isentropically to peak pressure. The Omega laser facility has the capacity for delivering 2-3 kJ of laser energy onto the front of our target reservoirs. These energy levels will generate sample pressures in excess of 1 Mbar. Experiments are currently underway for measuring strength in vanadium samples at pressures up to 1 Mbar. To reach

pressures in excess of 10 Mbar will require a MJ-class laser. Designs are in hand [24] for ultrahigh pressure strength experiments to be performed at the National Ignition Facility. This facility will be able to generate long laser pulses (> 40 ns) at total energies approaching 2 MJ. While there is a modest body of literature for dynamic strength work below 1 Mbar²⁵⁻²⁸, only a handful of experiments have attempted to measure the material strength at pressures approaching 1 Mbar.²⁹⁻³² To achieve quasi-isentropic states in solids at these pressures, it is critical that the sample material remain below the melt temperature. This requires that the drive remain shock-free throughout the sample volume. Maintaining shock-free loading for non-convergent drive geometries requires that the loading rate be faster than natural relaxation processes but not so fast that the compression wave evolves into a strong shock. At ultrahigh pressures, this will be the great experimental challenge.

VII. SUMMARY

In summary, we have started an effort to develop a materials science experimental testbed at ultrahigh pressures and strain rates. The “drive” to create these high pressure, solid-state conditions uses a reservoir-gap-sample configuration. This plasma piston, quasi-isentropic drive has been demonstrated thoroughly on the Omega laser at peak pressures spanning 0.1-2 Mbar, and strain rates covering $10^6 - 10^8$ s⁻¹. As an initial focus, we are developing the ability to infer material strength at extreme pressures, using modifications to the growth rate of the Rayleigh-Taylor (RT) instability. Initial results from RT experiments on the Omega laser at a peak pressure of 200 kbar are given, showing strong stabilization effects due to strength. Simulations show that this approach to high-pressure materials science will allow solid-state dynamics at pressures well in excess of 10 Mbar to be achieved, and high-pressure strength to be inferred in a variety of materials, on the NIF laser.

ACKNOWLEDGEMENTS

This work was performed under the auspice of the U.S. Department of Energy by the University of California, Lawrence Livermore National Laboratory under contract No. W-7405-Eng-48

REFERENCES

- ¹. M. J. Edwards, K. T. Lorenz, et al., *Phys. Rev. Lett.* (2004) In press.
- ². D. J. Steinberg, S. G. Cochran and M. W. Guinan, *J. Appl. Phys.* **51**, 1498 (1980).
- ³. T. J. Ahrens, K. G. Holland and G. Q. Chen, *Geophys. Res. Lett.* **29**, 54 (2002).
- ⁴. T. Guillot, *Science* **286**, 72 (1999).
- ⁵. J. F. Barnes, P. J. Blewett, R. G. McQueen, K. A. Meyer and D. Venable, *J. Appl. Phys.* **45**, 727 (1974).
- ⁶. A. I. Lebedev, P. N. Nisovtev and V. A. Rayevsky, "Rayleigh-Taylor instability in solids" in *Proceedings of the 4th Int. Workshop on the Physics of Compressible Turbulent Mixing*, Cambridge, England (1993).
- ⁷. V. A. Rayevsky, "RT instability effects in the acceleration of a plane solid layer" in *Proceedings of the 5th Int. Workshop on the Physics of Compressible Turbulent Mixing*, Ed. by R. Young J. Glimm and B. Boston, World Scientific, (1995).
- ⁸. A. I. Lebedev, P. N. Nisovtev, V. A. Rayevsky and V. P. Solovyov, "RT instability in strong media, experimental study" in *Proceedings of the 5th Int. Workshop on the Physics of Compressible Turbulent Mixing*, Ed. by R. Young J. Glimm and B. Boston, World Scientific, (1995).
- ⁹. A. I. Lebedev, P. N. Nisovtev, V. A. Rayevsky and V. P. Soloviov, "RT instability in strong substances: calculated experimental studies of instability in titanium" in *Proceedings of the 6th Int. Workshop on the Physics of Compressible Turbulent Mixing*, Marseille, France, Ed. by G. Jourdan and L. Houas, (1997).
- ¹⁰. V. A. Rayevsky, et al., "Research into RT instability in solids loaded to ~70 GPa" in *Proceedings of the 7th Int. Workshop on the Physics of Compressible Turbulent Mixing*, St. Petersburg, Russia, Ed. by E. Meshkov, Yu. Yanilkin and V. Zhmailo (1999).
- ¹¹. J. Colvin, M. Legrand, B. A. Remington, G. Schurtz and S. V. Weber, *J. Appl. Phys.* **93**, 5287 (2003).
- ¹². K. Mikaelian, *Phys. Rev. E* **54**, 3676 (1996).

13. O. L. Landen, D. R. Farley, S. G. Glendinning, L. M. Logory, P. M. Bell, J. A. Koch, F. D. Lee, D. K. Bradley, D. H. Kalantar, C. A. Back, R. E. Turner, *Rev. Sci. Instrum.* **72**, 627 (2001).
14. J. W. Swegle and A. C. Robinson, *J. Appl. Phys.* **66**, 2838 (1989).
15. G. B. Zimmerman and W. L. Kruer, *Comments Plasma Phys. Control. Fusion* **2**, 51 (1975).
16. P. M. Celliers, G. W. Collins, L. B. Da Silva, D. M. Gold and R. Cauble, *Appl. Phys. Lett.* **73**, 1320 (1998).
17. D. B. Hayes, "Backward Integration of the Equations of Motion to Correct for Free Surface Perturbations", Sandia National Laboratories Report SAND2001-1440 (2001).
18. D. B. Hayes, C. A. Hall J. R. Asay and M. D. Knudson, *J. Appl. Phys.* (2004), in press.
19. K. S. Budil, T. S. Perry, S. A. Alvarez, D. Hargrove, J. R. Mazuch, A. Nikitin and P. M. Bell, *Rev. Sci. Instrum.* **68**, 796 (1997).
20. B. A. Remington, S. V. Weber, M. M. Marinak, S. W. Haan, J. D. Kilkenny and R. J. Wallace, *Phys. Plasmas* **2**, 241(1995).
21. H. F. Robey, K. S. Budil and B. A. Remington, *Rev. Sci. Instrum.* **68**, 792 (1997).
22. D. K. Bradley, P. M. Bell, O. L. Landen, J. D. Kilkenny and J. Oertel, *Rev. Sci. Instrum.* **66**, 716 (1995).
23. R. E. Turner, O. L. Landen, D. K. Bradley, S. S. Alavarez, P. M> bell, R. Costa, J. D. Morley and D. Lee, *Rev. Sci. Instrum.* **72**, 706 (2001) and references therein.
24. B. A. Remington, *Astrophys. and Space Science*, July 2005, in press.
25. Yu. V. Bat'kov, V. N. Knyazen, S. A. Novikov, V. A. Rayevsky and N. D. Fishman, *J. Phys. IV France* **10**, Pr9-793 (2000).
26. J. W. Swegle, "Heterogeneous deformation models for the high pressure strength of aluminum" in *Proceedings of the American Physical Society Topical Conference on Shock Waves in Condensed Matter*, Ed. by S. C. Schmidt and N. C. Holmes, Elsevier (1988).

- ²⁷. J. R. Asay and J. Lipkin, *J. Appl. Phys.* **49**, 4242 (1978).
- ²⁸. J. R. Asay, L. C. Chhabildas and D. P. Dandekar, *J. Appl. Phys.* **51**, 4774 (1980).
- ²⁹. J. R. Asay, L. C. Chhabildas, T. G. Trucano and G. I. Kerley, "High Pressure Strength of Shocked Aluminum", in *Proceedings of the American Physical Society Topical Conference on Shock Waves in Condensed Matter* (1985).
- ³⁰. L. C. Chhabildas, J. R. Asay and L. M. Barker, Sandia National Laboratories Report SAND88-0306 (1988).
- ³¹. L. C. Chhabildas and L. M. Barker, Sandia National Laboratories Report SAND86-1888 (1986).
- ³². J. R. Asay, *Int. J. Impact Engng.* **20**, 27 (1997).

TABLE CAPTION

Table 1 – Details of laser and target specifications. (a) Drive calibration shots, (b) RT growth shots, (c) reservoirs not individually measured – used average values for 9 other target reservoirs fabricated in identical manner, (d) RT image recorded on CCD camera, (e) RT image recorded on optical film.

FIGURE CAPTIONS

Figure 1 – P-T phase diagram showing various paths to high-pressure solid states in aluminum. The melt temperature is calculated using a Lindemann melt law. The Hugoniot defines the end-states for single-shock loading. The laser technique outlined in this paper can generate shockless loading to multi-megabar, quasi-isentropic states.

Figure 2 – (a) Schematic diagram showing growth of a Rayleigh-Taylor (RT) instability in a plate under load. (b) Calculation of RT growth in Al-6061-T6 at a pressure of 200 kbar as a function of wavelength based on Eq. (2). The solid line shows the case for a plate having no material strength. For plates exhibiting strength, growth rates are reduced and exhibit a maximum growth wavelength. Y_0 is the zero-pressure yield strength (2.9 kbar) for Al-6061-T6.

Figure 3 – Schematic diagram showing the target-laser geometry for drive calibration (upper panel) and RT growth experiments (lower panel).

Figure 4 – (a) Optical micrograph of Al-6061-T6 stock from which RT target foils were machined. Dark spots are inclusions. Lighter and darker patches show outlines of the grain structure in the material. The length gauge in the lower left corner indicates 200 μm . (b) Cross-section of target foil used in RT growth experiments. Sinusoidal perturbations were machined into foil using single-point diamond turning. A thin coating of epoxy (finished thickness = 4.6 μm) was applied to the perturbation side as a heat shield. The epoxy was then machined to a flat surface.

Figure 5 – (a) Radiograph of gold SEM grid used for purposes of calibrating the x-ray camera resolution and magnification. Gold wires (dark lines) are 21 μm thick and spacing is 63.5 μm (wire center to wire center). (b) The modulation transfer function (MTF) extracted from Au grid radiograph. The MTF indicates how well an imaging system can reproduce an array of alternating light and dark lines. Perfect reproduction equals 1. Our x-ray camera reproduced about half of the actual contrast for the 40 μm target-foil perturbations.

Figure 6 – (a) Line VISAR record for drive calibration shot. The VISAR fringes record target velocity change as a function of time and position on the target.

One fringe jump is equivalent to 640 m/s. (b) Plot shows particle velocity of Al-LiF interface on back of target foil (solid line) extracted from VISAR record. The dotted line shows the applied pressure on the front of the target foil, based on back-integration of particle velocity data (see text). The dashed line shows a hydrocode simulation of the applied drive pressure.

Figure 7 – 1D and 2D calculated drive pressures on target foils. Dot-dash: 1D, front of foil. Dash: 1D, 5 μm inside front drive surface. Solid: 2D, front of foil. Dotted: 2D, 5 μm inside front drive surface.

Figure 8 – (a) In-flight x-ray radiograph of driven foil (shot 37019). Alternating lines show RT perturbations at $t_0 + 130$ ns (~ 90 ns after initial push). Lineout at right was averaged over the entire image. Lineouts used for RT growth analysis averaged over a 400 μm target region (indicated by the dotted box on the radiograph). (b) Plot showing a 1D Fourier transform (FFT) of the image in (a), which represents the differential optical density between peaks and valleys in the radiograph. From this, we deduce the RT growth as a function of wavelength and time.

Figure 9 – Experimental and calculated RT growth factors (GFs). The plot shows measured increases in the perturbation amplitude of the foils for five times. Times and GFs are listed in Table 1 along with values for the error bars. Dotted line shows the calculated growth of the perturbations for Al-6061-T6 having no material strength (liquid behavior). The other lines indicate reduction in growth as a function of increased material strength. The dashed line shows the calculated RT growth using a Steinberg-Guinan model (Eq. 7). The solid lines show calculated RT growth for increasing amounts of pressure hardening, where the A-term in Eq. 7 was multiplied by factors of 0.7, 1.5 and 2.0.

Figure 10 – The dynamic strength enhancement of Al-6061-T6 at a peak pressure of 200 kbar. The solid line shows the calculated dynamic strength (from Eq. 7) divided by the yield point, Y_0 . The dashed line shows the calculated drive pressure applied to the RT target foils. The dynamic strength is enhanced by a factor of $\sim 2.5\times$ over ambient conditions, and closely follows the pressure history on the foil. Note also the residual late-time strength due to strain hardening.